Linear and nonlinear optical properties of Ag/Au bilayer thin films

James Hsu,[1] Canek Fuentes-Hernandez,[1] Alfred R. Ernst,[1] Joel M. Hales,[2] Joseph W. Perry,[2] and Bernard Kippelen[1,*]

[1]*Center for Organic Photonics and Electronics, School of Electrical and Computer Engineering, Georgia Institute of Technology, Atlanta, GA 30332-0250, USA*
[2]*Center for Organic Photonics and Electronics, School of Chemistry and Biochemistry, Georgia Institute of Technology, Atlanta, GA 30332-0400, USA*
**kippelen@gatech.edu*

Abstract: The linear and nonlinear optical properties of Ag/Au bilayer metallic thin films with a total thickness of around 20 nm and with different Ag/Au mass-thickness ratios were studied. This study shows that the spectral dispersion of the effective refractive index of bilayer films can be tuned by controlling the mass-thickness ratio between Au and Ag. Improvement of the figure-of-merit for potential plasmonic applications and linear optical filters in the visible spectral range are reported and discussed. The nonlinear optical properties of bilayer metal films studied using femtosecond white-light continuum pump-probe experiments are also shown to be tunable with this ratio. The nonlinear change of optical path length is extracted from the pump-probe data and agrees with simulated values derived from a combination of the two-temperature model, describing the ultrafast electron heating dynamics, and a physical model that describes the dielectric permittivity of Au as a function of electron and lattice temperature.

OCIS codes: (160.3900) Metals; (310.6860) Thin films, optical properties; (300.6500) Spectroscopy, time-resolved; (240.6680) Surface plasmons.

References and links

1. W. L. Barnes, A. Dereux, and T. W. Ebbesen, "Surface plasmon subwavelength optics," Nature **424**(6950), 824–830 (2003).
2. H. T. Chen, W. J. Padilla, J. M. O. Zide, A. C. Gossard, A. J. Taylor, and R. D. Averitt, "Active terahertz metamaterial devices," Nature **444**(7119), 597–600 (2006).
3. D. T. Owens, C. Fuentes-Hernandez, J. M. Hales, J. W. Perry, and B. Kippelen, "Nonlinear optical properties of induced transmission filters," Opt. Express **18**(18), 19101–19113 (2010).
4. M. J. Bloemer and M. Scalora, "Transmissive properties of Ag/MgF2 photonic band gaps," Appl. Phys. Lett. **72**(14), 1676–1678 (1998).
5. S. Y. Ryu, C. H. Lee, I. S. Oh, S. Y. Song, K. H. Hwang, H. S. Hwang, M. H. Han, B. H. Hwang, H. K. Baik, Y. S. Kim, and J. Y. Lee, "Efficient inverted top-emitting organic light emitting diodes with transparent and surface-modified multilayer anodes," Electrochem. Solid-State Lett. **13**(5), J43–J46 (2010).
6. N. Rotenberg, A. D. Bristow, M. Pfeiffer, M. Betz, and H. M. van Driel, "Nonlinear absorption in Au films: Role of thermal effects," Phys. Rev. B **75**(15), 155426 (2007).
7. D. T. Owens, C. Fuentes-Hernandez, J. M. Hales, J. W. Perry, and B. Kippelen, "A comprehensive analysis of the contributions to the nonlinear optical properties of thin Ag films," J. Appl. Phys. **107**(12), 123114 (2010).
8. M. A. Swillam, N. Rotenberg, and H. M. van Driel, "All-optical ultrafast control of beaming through a single sub-wavelength aperture in a metal film," Opt. Express **19**(8), 7856–7864 (2011).
9. G. A. Wurtz, R. Pollard, W. Hendren, G. P. Wiederrecht, D. J. Gosztola, V. A. Podolskiy, and A. V. Zayats, "Designed ultrafast optical nonlinearity in a plasmonic nanorod metamaterial enhanced by nonlocality," Nat. Nanotechnol. **6**(2), 107–111 (2011).
10. N. Rotenberg, M. Betz, and H. M. van Driel, "Ultrafast all-optical coupling of light to surface plasmon polaritons on plain metal surfaces," Phys. Rev. Lett. **105**(1), 017402 (2010).
11. J. Y. Zhang, L. Wang, S. Krishna, M. Sheik-Bahae, and S. R. J. Brueck, "Saturation of the second harmonic generation from GaAs-filled metallic hole arrays by nonlinear absorption," Phys. Rev. B **83**(16), 165438 (2011).

#163236 - $15.00 USD Received 22 Feb 2012; revised 16 Mar 2012; accepted 19 Mar 2012; published 28 Mar 2012

12. S. I. Anisimov, B. L. Kapeliovich, and T. L. Perel'Man, "Electron emission from metal surfaces exposed to ultrashort laser pulses," Sov. Phys. JETP **39**, 375–377 (1974).
13. C. Voisin, N. Del Fatti, D. Christofilos, and F. Vallee, "Ultrafast electron dynamics and optical nonlinearities in metal nanoparticles," J. Phys. Chem. B **105**(12), 2264–2280 (2001).
14. P. E. Hopkins, "Influence of Inter- and Intraband Transitions to Electron Temperature Decay in Noble Metals After Short-Pulsed Laser Heating," J. Heat Transfer **132**(12), 122402 (2010).
15. B. H. Ong, X. C. Yuan, and S. C. Tjin, "Bimetallic silver-gold film waveguide surface plasmon resonance sensor," Fiber Integr. Opt. **26**(4), 229–240 (2007).
16. H. Tóháti, A. Sipos, G. Szekeres, A. Mathesz, A. Szalai, P. Jojart, J. Budai, C. Vass, A. Kohazi-Kis, M. Csete, and Z. Bor, "Surface plasmon scattering on polymer-bimetal layer covered fused silica gratings generated by laser induced backside wet etching," Appl. Surf. Sci. **255**(10), 5130–5137 (2009).
17. M. Thomschke, S. Hofmann, S. Olthof, M. Anderson, H. Kleemann, M. Schober, B. Lussem, and K. Leo, "Improvement of voltage and charge balance in inverted top-emitting organic electroluminescent diodes comprising doped transport layers by thermal annealing," Appl. Phys. Lett. **98**(8), 083304 (2011).
18. T. Q. Qiu, T. Juhasz, C. Suarez, W. E. Bron, and C. L. Tien, "Femtosecond laser heating of multi-layer metals—II. Experiments," Int. J. Heat Mass Transfer **37**(17), 2799–2808 (1994).
19. T. Q. Qiu and C. L. Tien, "Femtosecond laser heating of multi-layer metals—I. Analysis," Int. J. Heat Mass Transfer **37**(17), 2789–2797 (1994).
20. W. J. Scouler, "Temperature-modulated reflectance of gold from 2 to 10 ev," Phys. Rev. Lett. **18**(12), 445–448 (1967).
21. M. G. Blaber, M. D. Arnold, and M. J. Ford, "A review of the optical properties of alloys and intermetallics for plasmonics," J. Phys. Condens. Matter **22**(14), 143201 (2010).
22. H. A. Macleod, "The induced-transmission filter," in *Thin-Film Optical Filters,* 3rd ed. (Institute of Physics Publishing, London, 2001).
23. Z. Lin, L. V. Zhigilei, and V. Celli, "Electron-phonon coupling and electron heat capacity of metals under conditions of strong electron-phonon nonequilibrium," Phys. Rev. B **77**(7), 075133 (2008).
24. J. Y. Bigot, J. Y. Merle, O. Cregut, and A. Daunois, "Electron dynamics in copper metallic nanoparticles probed with femtosecond optical pulses," Phys. Rev. Lett. **75**(25), 4702–4705 (1995).
25. P. G. Etchegoin, E. C. Le Ru, and M. Meyer, "An analytic model for the optical properties of gold," J. Chem. Phys. **125**(16), 164705 (2006).

1. Introduction

Noble metals, such as gold and silver, have a wide range of applications in photonics and electro-optics. Within the visible and infrared spectral regions, gold and silver can have a negative permittivity that allows for the excitation of surface plasmon polaritons (SPPs), which have been actively exploited in recent years for sub-wavelength photonic circuits [1]. This negative permittivity also enables artificial metamaterial structures which allow remarkable control over the dispersion and sign of the refractive index of a material and consequently over the flow of electromagnetic energy throughout its structure [2]. In addition, highly transparent metallic structures [3] have been reported and are attractive as optical filters with high out-of-band rejection [4] and thin film metal electrodes in organic light-emitting diodes [5]. Noble metals have also attracted great attention because their extremely large and ultrafast non-linear optical (NLO) response [6,7] can be exploited to achieve all-optical control of metallic nanostructures [8–11]. This NLO response is described as a $\chi^{(1)}$ process caused by electron and lattice heating [6,7,12].

The linear and nonlinear optical responses of a noble metal and their potential applications are therefore determined by the inherent electronic response which gives rise to their dielectric permittivity. The electronic response of a noble metal in the visible spectral region can be divided into two separate mechanisms: interband and intraband electronic transitions [13,14]. Electronic interband transitions in the visible or ultraviolet (UV) spectral region arise from bound electrons excited from fully occupied electronic states within the d-band, below the Fermi energy level, to the half filled s-p electronic bands in the conduction band. In this spectral region, metals are opaque because optical fields are strongly absorbed. At lower energies, electronic intraband transitions occur from free electrons stimulated within the conduction band. In this spectral region, metals are opaque mainly because the optical fields are reflected off its surface, rather than absorbed in the bulk.

When a metal is excited with an ultrafast optical pulse, the energy absorbed by the electron gas raises its temperature and smears the electronic distribution around the Fermi

#163236 - $15.00 USD Received 22 Feb 2012; revised 16 Mar 2012; accepted 19 Mar 2012; published 28 Mar 2012

energy (Fermi-smearing), causing a very strong change of the dielectric permittivity of the metal around the onset of interband region [13]. In the intraband region, an increased electron temperature increases electron scattering processes which change the dielectric permittivity, albeit these changes are of smaller magnitude than the ones produced in the onset of the interband region [7]. Therefore, gold and silver have very different linear and nonlinear optical properties not only because of inherent differences in their electronic configurations, but also because these differences cause the onset of interband transitions to lie in very different spectral regions (in the visible for gold and in the UV for silver).

Although silver and gold are commonly used as single component materials, configurations of Ag/Au bilayer thin films have also been used to solve multiple engineering problems. For instance, high chemical stability and high sensor sensitivity have been achieved by using Ag/Au bilayer films in different surface plasmon resonance (SPR) sensor designs [15,16]. Al/Ag bilayer films have also been used as transparent electrodes in top-emitting organic light-emitting diodes [17]. Additionally, the interactions between multi-layer metal films and femtosecond laser pulses have been studied in terms of increasing the damage threshold of laser mirrors [18,19]. However, little attention has been directed at understanding the linear and nonlinear optical properties of Ag/Au bilayer thin films by controlling the thickness ratio between the two metals.

In this paper, the linear and nonlinear optical properties of Ag/Au bilayer metallic thin films with a total thickness of around 20 nm and with different Ag/Au mass-thickness ratios were studied. This study shows that the spectral dispersion of the effective refractive index of bilayer films preserves the general dispersion features found in their component materials, namely distinct interband-like and intraband-like transition regions. In addition, it is also shown that the effective refractive index can be tuned spectrally by controlling the mass-thickness ratio between gold and silver. As a consequence, it is shown that the magnitude and spectral dispersion for the NLO response of the bilayer films can also be tuned. These changes are modeled using the two-temperature model and a physical model that describes the dielectric permittivity in terms of their interband and intraband transition terms. Potential linear and nonlinear optical applications of these metallic bilayers are also discussed.

2. Experimental method

2.1 Fabrication and characterization

All thin films were deposited on Ted Pella Micro Cover Glass substrates with a Kurt. J Lesker Axxis electron beam deposition system. Substrates were cleaned ultrasonically in deionized water, acetone and isopropanol for 15 min each. The films were deposited under vacuum at a pressure of 8.5×10^{-7} Torr (1.1×10^{-4} Pa) with a rotating sample holder that actively cools the substrates to room temperature. The Ag and Au were deposited at a rate of 0.1 nm/s and SiO_2 was deposited at a rate of 0.5 nm/s, monitored by crystal sensors.

Ag/Au bilayer thin films were fabricated by deposition of the Ag layer onto a glass substrate followed by the deposition of the Au layer. Such bilayer films were sandwiched by SiO_2 thin films as protection layers. Bilayers with three thickness ratios of Au and Ag with a total thickness of 20 nm were fabricated. Single layers of Au and Ag were fabricated as reference samples with the same total thickness. Single layer and bilayer metallic samples with the following geometry were deposited:

R1: Glass/*Au* (23 nm).

S1: Glass/SiO_2(64 nm)/ *M1*/SiO_2(98 nm).

S2: Glass/SiO_2(64 nm)/ *M2*/SiO_2(98 nm).

S3: Glass/SiO_2(64 nm)/ *M3*/SiO_2(98 nm).

R2: Glass/*Ag* (20 nm).

#163236 - $15.00 USD Received 22 Feb 2012; revised 16 Mar 2012; accepted 19 Mar 2012; published 28 Mar 2012

where *Au* and *Ag* corresponds to a 23 nm and 20 nm thick Au and Ag film, respectively, and *M1* corresponds to Ag(4 nm)/Au(14 nm), *M2* to Ag(10 nm)/ Au(10 nm) and *M3* to Ag(15 nm)/ Au(6 nm) bilayers. The layer thicknesses (shown inside the parentheses) were individually estimated by matching transfer matrix method simulations with measured values of the transmittance (*T*), reflectance (*R*), and absorptance (*A*) spectra taken by a Shimadzu UV-Vis-NIR scanning spectrophotometer. Refractive index values of deposited *Au* and *Ag* films were obtained by modeling spectroscopic ellipsometric (SE) data (J.A. Woollam M-2000UI), taken on individual films, as a perfectly flat continuous layer. The effective refractive indices ($N_{eff} = n_{eff} + ik_{eff}$) of the bilayer films were calculated from SE data imposing Kramers-Kronig consistency to the calculated values.

The nonlinear optical properties (NLO) of these films were characterized by a commercially available white-light continuum (WLC) pump-probe spectroscopy system (Helios, ultrafast system). The pump pulse obtained from an optical parametric amplifier (TOPAS-C, Spectra-Physics) was tuned to a wavelength of 560 nm. A laser beam from a Ti:Sapphire regenerative amplifier (Spitfire, Spectra-Physics) operating at 800 nm pumped the TOPAS-C, while a small portion of this beam generated the WLC (420 - 950 nm) probe pulse. The WLC probe pulse measured 60 μm half-width-1/e (HW 1/e) at the sample position using a knife-edge scan, and the pump pulse was 285 μm (HW 1/e). Because the probe size is significantly smaller than the pump, it is assumed that the probe overlaps with a region of approximately constant peak fluence from the pump. The pump has a pulse width of 60 fs (HW 1/e) and the total instrument response time is 150 fs full-width-half-maximum (FWHM). The pump beam was chopped at 500 Hz with a 50% duty cycle to obtain pumped (signal) and non-pumped (reference) probe spectra sequentially. After averaging over one thousand probe pulses at each time delay, the change in optical density ($\Delta OD(\lambda, t)$) was recorded as a function of wavelength (λ) and delay time (t). The fluence of the probe pulses for all samples was confirmed to be low enough to produce no observable NLO response. Scattered pump light was subtracted from the data based on measurements at negative delay times. A temporal correction factor was applied to all data sets to provide equivalent zero delay onsets for all probe wavelengths; this correction factor was determined by measuring the chirp of the WLC probe passing through the glass substrate. The transmittance spectra change ($\Delta T(\lambda, t)$) and reflectance spectra change ($\Delta R(\lambda, t)$) of the WLC probe pulses were calculated from measured $\Delta OD(\lambda, t)$ as a function of delay time for a variety of pump fluences by $\Delta T(\lambda,t) = -\ln(10)T\left(\Delta OD(\lambda,t)\right)$ and $\Delta R(\lambda,t) = -\ln(10)R\left(\Delta OD(\lambda,t)\right)$, where T and R are the linear transmittance and reflectance spectra, respectively. This formula is derived from a Taylor series expansion and therefore is only valid for small values of $\Delta OD(\lambda, t)$.

3. Results and discussion

3.1. Linear optical properties

Figure 1, shows a comparison of the measured *T*, *R* and *A* spectra (symbols) on all samples and the simulated spectra following two different approaches. In the first approach, referred to as linear model 1 (thin lines), the optical properties of the Ag/Au bilayers were modeled as two continuous layers with uniform thickness, each with refractive index values obtained from the analysis of SE data on samples **R1** and **R2**. The mean square error (MSE) values of the fits to the SE data are 5.7 and 4.7 for samples **R1** and **R2**, respectively. Following this approach a fair description of the optical properties of the bi-metal layers can be obtained. The discrepancy between experimental and simulated spectra is worst for sample **S1,** likely because the bottom 4 nm Ag film is expected to be non-continuous, resulting in a very rough top (14 nm) Au layer and differing significantly from the assumptions made in the model. In the second approach, referred to as linear model 2 (thick lines), each N_{eff} and thickness (shown inside the parenthesis) of bilayers for samples **S1** (*M1* 24 nm), **S2** (*M2* 20 nm), and **S3** (*M3* 24 nm) were extracted from SE data using a single layer model to describe the bi-metal (without

#163236 - $15.00 USD Received 22 Feb 2012; revised 16 Mar 2012; accepted 19 Mar 2012; published 28 Mar 2012

surface roughness). The MSE values of the fits to the SE data are 5.2, 5.5 and 5.0 for samples **S1**, **S2** and **S3**, respectively. These N_{eff} values were then used to simulate the *T*, *R* and *A* spectra. This single layer model yields better agreement between simulated and measured values in sample **S1**, since it bypasses the morphological details of the Ag/Au interface.

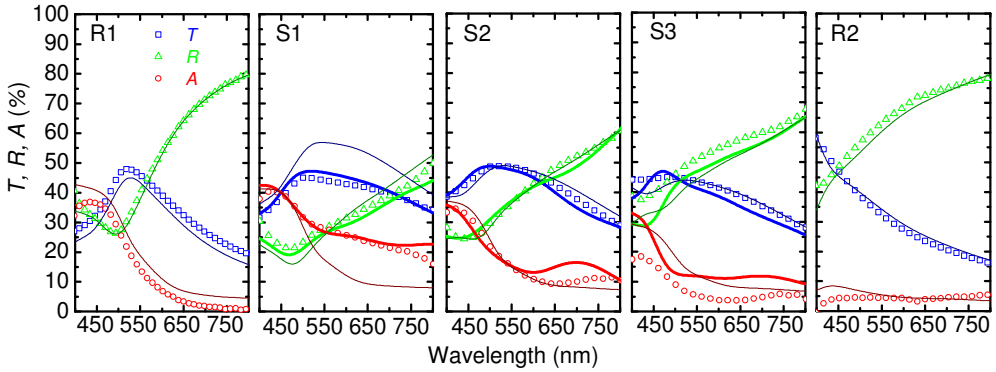

Fig. 1. Comparison of measured (symbols) and simulated (linear model 1: thin lines, linear model 2: thick lines) transmittance (*T*) (blue), reflectance (*R*) (green) and absorptance (*A*) (red) spectra in the visible range for fabricated samples **R1**, **S1**, **S2**, **S3** and **R2.**

Figures 2(a) and 2(b) show the N_{eff} values of bilayers *M1*, *M2* and *M3*, as well as the refractive index values of single layer *Au* and *Ag*. For *Au* and *Ag*, the index values are close to literature values, with the interband transition onset of bulk Au [20] located at 520 nm and the interband transition onset of bulk Ag [13] at 313 nm. At these wavelengths, inflection points are present in the real part of refractive index. In contrast, for *M1*, *M2* and *M3* the inflection point in N_{eff} in the visible range moves away from *Au* and towards *Ag* as the thickness ratio of Au to Ag decreases, resulting in an apparent blue shift of the onset of interband transitions (Fig. 2(a)). In other words, by controlling the Ag/Au mass thickness ratio in these bilayers metallic films, the apparent onset of interband transitions can be spectrally tuned. This tunability, as will be described next, can be attractive for a variety of linear and nonlinear applications.

Two figures-of-merit or quality factors have been recently introduced by Blaber, et al. [21] to evaluate the potential of metals for plasmonic applications. The first quality factor (Q_{LSP}) relates to the proficiency of a metal, with dielectric permittivity $\varepsilon = \varepsilon' + i\varepsilon''$, to sustain localized surface plasmon (LSP) excitations. Q_{LSP} is defined by the ratio $-\varepsilon' / \varepsilon''$, which can be directly related to, for instance, the resolving power of a single layer or multilayer superlens. The second quality factor (Q_{SPP}) relates to the proficiency of a metal to sustain surface plasmon polartions (SPP). Q_{SPP} is defined by the ratio $(\varepsilon')^2 / \varepsilon''$, which is directly related to the propagation length of SPPs in plasmonic waveguides.

Figures 2(c) and 2(d) shows the spectral dispersion of Q_{LSP} and Q_{SPP} calculated for *M1*, *M2*, *M3*, *Au* and *Ag*. The permittivity of each film was calculated from the $N_{eff} = \varepsilon^{1/2}$ values (Figs. 2(a) and 2(b)). Note that *Au* always displays lower quality factors Q_{LSP} and Q_{SPP} values than *Ag*. Strong absorptive losses in *Ag* due to interband transitions limit Q_{LSP} and Q_{SPP} values in the UV wavelength range from 250 to 350 nm. For *Au*, the same mechanism also limits the values of Q_{LSP} and Q_{SPP} in the wavelengths range from 250 to 500 nm. In this wavelength range, the apparent tuning of the onset of interband transitions achieved by decreasing the mass thickness ratio of Au to Ag leads to higher Q_{LSP} and Q_{SPP} values for all bilayer Ag/Au films compared to *Au*. For instance, at wavelength 490 nm, Q_{LSP} improves from a value of 0.47 for *Au*, to values of 0.79 for *M1*, 2.3 for *M2*, and 4.5 for *M3*. In contrast, at this wavelength Q_{LSP} = 9.8 for *Ag*. Similarly, at 490 nm, Q_{SPP} improves from a value of 0.89 for *Au*, to values of 1.9 for *M1*, 11 for *M2*, and 23 for *M3*, while for Ag it has a value of 78. Although for wavelengths above ~600 nm, the quality factors for Au are higher than for any

#163236 - $15.00 USD Received 22 Feb 2012; revised 16 Mar 2012; accepted 19 Mar 2012; published 28 Mar 2012

of the bilayers. It is interesting to note that in the range from 825 to 950 nm, *M2* shows Q_{LSP} and Q_{SPP} values that are again higher than *Au* and even higher than *Ag*. Hence, although for linear plasmonic applications Ag displays higher quality factors in general, for applications that would require ultrafast all-optical plasmonic control [10], the bilayers will offer a very attractive combination of properties since the NLO response of any of the bilayers is significantly larger than that of Ag, as described in the next section. Finally, it should be noted that the values of N_{eff} and consequently Q_{LSP} and Q_{SPP} are dependent on the metallic film morphology, which is dependent on the conditions for the deposition of these metallic films. Hence, the results described here represent only general trends to be expected for a given deposition process.

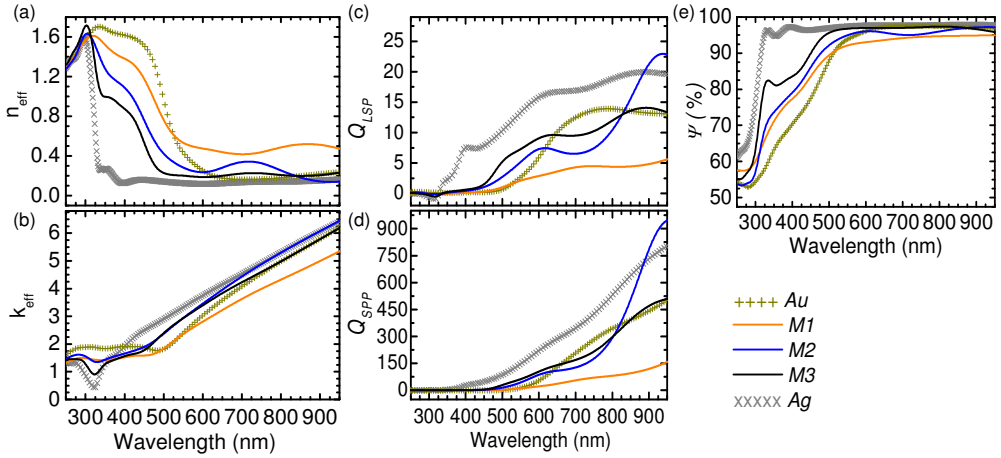

Fig. 2. (a) Real and (b) imaginary effective refractive index values of bilayer Ag/Au metal thin films: *M1*, *M2* and *M3*; *Au* and *Ag* are shown as reference. (c) Quality factor spectra for localized surface plasmon and (d) quality factor spectra for surface plasmon polariton. (e) Simulated maximum potential transmittance spectra.

For applications of Au/Ag bilayer films in linear optical filters, such as band pass filters (metal-dielectric band gap structures, induced transmission filters, etc.) or as transparent electrodes in electro-optic devices, the concept of maximum potential transmittance is useful since it provides an upper limit to the transmittance of an absorbing film, after all reflectance losses are suppressed., The maximum potential transmittance, Ψ, for a single metallic film is defined by the following equation [22]

#163236 - $15.00 USD Received 22 Feb 2012; revised 16 Mar 2012; accepted 19 Mar 2012; published 28 Mar 2012

$$\psi = \left(\begin{array}{l} \dfrac{(n^2 - k^2 - 2nk(Z/X))}{(n^2 + k^2)} (\sin^2\alpha \cos\mathrm{h}^2\beta + \cos^2\alpha \sin\mathrm{h}^2\beta) + (\cos^2\alpha \cos\mathrm{h}^2\beta + \sin^2\alpha \sin\mathrm{h}^2\beta) \\ + \dfrac{1}{X}(n \sin\mathrm{h}\beta \cos\mathrm{h}\beta + k \cos\alpha \sin\alpha) + \dfrac{X^2 + Z^2}{X(n^2 + k^2)}(n \sin\mathrm{h}\beta \cos\mathrm{h}\beta - k \cos\alpha \sin\alpha) \end{array} \right)^{-1}$$

with parameters $\alpha = 2\pi nd / \lambda$ and $\beta = 2\pi kd / \lambda$. X and Z are defined as

$$X = \left[\frac{(n^2 + k^2)(n \sin\mathrm{h}\beta \cos\mathrm{h}\beta + k \sin\alpha \cos\alpha)}{(n \sin\mathrm{h}\beta \cos\mathrm{h}\beta - k \sin\alpha \cos\alpha)} - \frac{n^2 k^2 (\sin^2\alpha \cos\mathrm{h}^2\beta + \cos^2\alpha \sin\mathrm{h}^2\beta)^2}{(n \sin\mathrm{h}\beta \cos\mathrm{h}\beta - k \sin\alpha \cos\alpha)^2} \right]^{\frac{1}{2}}$$

$$Z = \frac{nk(\sin^2\alpha \cos\mathrm{h}^2\beta + \cos^2\alpha \sin\mathrm{h}^2\beta)}{(n \sin\mathrm{h}\beta \cos\mathrm{h}\beta - k \sin\alpha \cos\alpha)} \tag{1}$$

where d is the layer thickness, λ is the free-space wavelength, and n and k are the real and imaginary parts of the refractive index, respectively.

In Fig. 2(e), the values of the maximum potential transmittance for *Ag*, *Au*, and bilayer films are compared by using the N_{eff} values previously derived and assuming films of equal thickness, 20 nm, to provide a fair comparison. Note that as a general statement, *Au* always displays lower values of Ψ than *Ag*. For wavelengths 350-500 nm, strong absorptive losses in *Au* due to interband transitions limits the values of Ψ compared to *Ag*, which has an interband transition region in the UV range. As expected from the apparent tuning of the onset of interband transitions, decreasing the ratio of Au to Ag leads to larger values of Ψ in all Ag/Au bilayer films compared to Au, in the 350-500 nm wavelength range. For instance, at wavelength 400 nm, Ψ improves from 70% for *Au* to 77% for *M1*, 79% for *M2*, and 84% for *M3*, as the thickness ratio of Au to Ag decreases (Fig. 2(e)). In the 500-950 nm range, bilayer films do not display improved values of Ψ but remain still higher than 90%. Once more, although Ag offers better linear optical properties across the visible spectrum, its more reactive nature to the environment and its much smaller NLO response make it less attractive for applications where improved environmental stability and higher NLO response are required.

3.2. Nonlinear optical properties

Potential applications for all-optical control that use the very large magnitude of the NLO response of noble metals, Au and Cu in particular, make it interesting to explore the NLO response of these bilayer films. The largest NLO response in a thin film of a noble metal arises due to the so-called Fermi smearing process. This process is driven by the rapid heating of electrons upon the absorption of energy from an ultrafast optical pulse. The rise of electronic temperature broadens the electronic distribution around the Fermi energy, at the onset of interband transitions, causing a drastic change of the dielectric permittivity of the metal [13].

Figures 3(a) and 3(b) show the values of $\Delta T(\lambda, t_{peak})$ and $\Delta R(\lambda, t_{peak})$ measured in pump-probe experiments in samples **R1**, **S1**, **S2** and **S3** for a pump fluence of 25 J/m^2. Figures 3(c) and 3(d) shows the temporal evolution of $\Delta T(\lambda_{peak} = 520\text{ nm}, t)$ and $\Delta R(\lambda_{peak} = 520\text{ nm}, t)$ measured on the same samples. Here, the subscript *peak* denotes the maximum value of the NLO response in the spectral and temporal ranges studied. For a single Ag layer, the

#163236 - $15.00 USD Received 22 Feb 2012; revised 16 Mar 2012; accepted 19 Mar 2012; published 28 Mar 2012

maximum $|\Delta T(\lambda, t_{peak})|$ and $|\Delta R(\lambda, t_{peak})|$ are at least an order of magnitude smaller (<0.5% for a pump fluence of 50 J/m^2) than those found in bilayer or single Au layer films [7], so their values are not included in Fig. 3. For bilayer films, **S1**, **S2**, and **S3**, the $\Delta T(\lambda, t_{peak})$ and $\Delta R(\lambda, t_{peak})$ spectra display similar dispersion characteristics found in a single Au layer (**R1**). Under the same incidence pump fluence, the peak-to-valley magnitude of $\Delta T(\lambda, t_{peak})$ and $\Delta R(\lambda, t_{peak})$ gradually reduces as the mass thickness ratio of Au to Ag decreases from **R1**, **S1**, **S2** to **S3** (Figs. 3(a) and 3(b)). Interestingly, there is a consistent blue-shift of the wavelength at which maximum values of $\Delta T(\lambda_{peak}, t_{peak})$ and $\Delta R(\lambda_{peak}, t_{peak})$ are observed: by decreasing the mass thickness ratio of Au to Ag, the $|\Delta T(\lambda_{peak}, t_{peak})|$, peak wavelength and magnitude, changes from $|\Delta T(513\text{ nm}, t_{peak})| = 7.8\%$ for **R1** to $|\Delta T(498\text{ nm}, t_{peak})| = 4.8\%$ for **S1**, $|\Delta T(496\text{ nm}, t_{peak})| = 2.5\%$ for **S2**, and $|\Delta T(490\text{ nm}, t_{peak})| = 0.7\%$ for **S3**. A similar trend is found for ΔR as shown in Fig. 3(b). The trend of these shifts is consistent with the shifts in the onset of interband transitions shown in Fig. 2(a). This correspondence shows that both linear and NLO properties can be tuned by controlling the mass-thickness ratio between Ag and Au in bilayer films, albeit the magnitude of the NLO changes appears to be reduced as the Ag content increases. This apparent reduction, as will be later described, arises primarily from differences in the absorbed power within the Au layer.

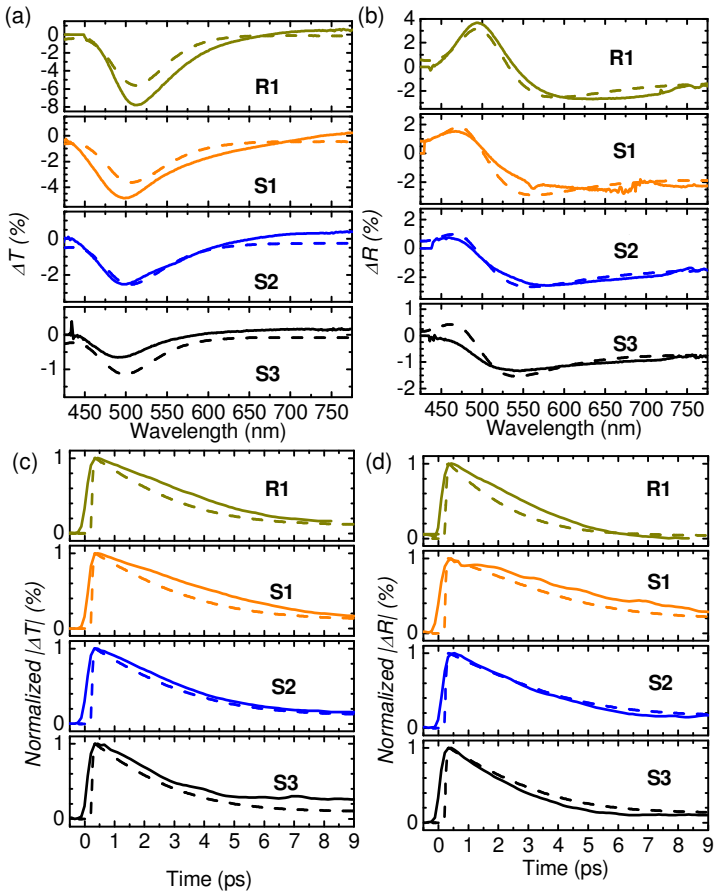

Fig. 3. (a), (b) Spectral dependence of transmittance and reflectance changes ($\Delta T(\lambda, t_{peak})$ and $\Delta R(\lambda, t_{peak})$) measured from WLC pump probe experiment (solid line) and simulation by two-temperature model (dashed line) of samples **R1**, **S1**, **S2** and **S3** with a pump fluence of 25 J/m^2; (c), (d) experimental (solid line) and simulated (dashed line) temporal dependence of the normalized absolute transmittance and reflectance changes probed at 520 nm. The excitation wavelength in all cases was 560 nm.

#163236 - $15.00 USD Received 22 Feb 2012; revised 16 Mar 2012; accepted 19 Mar 2012; published 28 Mar 2012

In order to gain a better understanding of the NLO properties of these bi-metal layers, the two-temperature model was introduced (Eq. (2)) to describe the heating of electrons and the lattice when optically pumped [7,13].

$$C_e\left(T_e\right)\frac{dT_e}{dt} = -G(T_e - T_l) + P(t)$$
$$C_l\frac{dT_l}{dt} = G(T_e - T_l) \tag{2}$$

The changes in electron and lattice temperatures calculated through the two temperature model depend upon intrinsic material properties such as the electron and lattice specific heats, C_e and C_l, respectively, and the electron phonon coupling constant, G, and are driven by the density of absorbed power within each individual layer $P(t)$. In our simulation $C_e(T_e) = (62 \pm 5) \times T_e$ [J/m^{3}K], $C_l = (3.2 \pm 0.4) \times T_e$ [J/m^{3}K], $G = (1.8 \pm 0.1) \times 10^{16}$ [W/m^{3}K] and the density of absorbed power is estimated as $P(t) = I(t)A/d$ [W/m^3], where $I(t)$ is the pump irradiance, here assumed to have a Gaussian temporal profile with a pulse width of 60 fs (HW 1/e); A is the linear absorptance in the metal layer, calculated using the transfer matrix method; and d is the thickness of the metal layer. These values were obtained by fitting $\Delta T(\lambda_{peak}, t)$ and $\Delta R(\lambda_{peak}, t)$, measured for an incident pump fluence of 8 J/m^2, with the physical model described in following paragraphs and show magnitudes that are comparable to literature values [6]. Here, we note that the linear approximation of C_e (T_e) and the temperature independent value of G are valid only in the low-fluence regime; this is, for electron temperatures smaller than around 3000 K for Au [23]. At the highest pump fluence of 25 J/m^2 used in this work, the maximum electron temperature in all samples is calculated to be between 1300 – 1500 K.

The electron and lattice temperatures derived from the two temperature model are used in a temperature-dependent physical model of the dielectric permittivity to calculate the complex refractive index changes $\Delta n_{sim}(\lambda, t)$ and $\Delta k_{sim}(\lambda, t)$.

For simplicity, the model implemented here to describe the NLO response of bilayers only accounts for the contribution of the Au component. This is motivated by the fact that only very minor adjustments were found when the contribution of Ag, as described in [7] was included in the calculations. The dielectric permittivity of Au, was modeled as a set of explicit equations (Eqs. (3)-(5)), as functions of frequency, temperature and time, via the superposition of a Drude-like intraband transition term (ε_{intra}) and an interband transition term (ε_{inter}) following Bigot, et al. [24], as follows

$$\varepsilon\left(\omega, T_l\left(t\right), T_e\left(t\right)\right) = \varepsilon_{intra}\left(\omega, T_l\left(t\right), T_e\left(t\right)\right) + \varepsilon_{inter}\left(\omega, T_e\left(t\right)\right) \tag{3}$$

Hereafter, ω is the free space optical frequency, t is the time, and $T_l(t)$ and $T_e(t)$ are dependent lattice and electron temperatures, respectively.

For the first term in Eq. (3),

$$\varepsilon_{intra}\left(\omega, T_l\left(t\right), T_e\left(t\right)\right) = 1 + \varepsilon_b - \frac{\omega_p^2}{\omega^2 + i\gamma\omega}$$

with parameters, (4)

$$\gamma\left[T_l(t), T_e(t)\right] = \gamma_0 + \gamma_1 \times T_l(t) + \gamma_2 \times T_e^{\,2}(t) + \gamma_3 \times \omega^2$$

where, ε_b is the background dielectric constant, γ is the damping constant, ω_p is the bulk plasma frequency, and γ_0, γ_1, γ_2, and γ_3 are constant coefficients [7].

For the second term in Eq. (3),

#163236 - $15.00 USD Received 22 Feb 2012; revised 16 Mar 2012; accepted 19 Mar 2012; published 28 Mar 2012

$$\varepsilon_{inter}\left(\omega,T_e\left(t\right)\right)=\sum_{j=1}^{M}\kappa_{(j)}\int_0^{\infty}dx\frac{\sqrt{x-E_{g(j)}}}{x^2}\left[1-F_{(j)}\left(x,T_e(t)\right)\right]\frac{\hbar^2\omega^2-x^2-\gamma_{ee(j)}^2-2i\hbar\omega\gamma_{ee(j)}}{\left(\hbar^2\omega^2-x^2-\gamma_{ee(j)}^2\right)^2+4\hbar^2\omega^2\gamma_{ee(j)}^2}$$

with parameters,

$$F_{(j)}(x,T_e(t))=\left(1+\exp\left(\frac{x-E_{f(j)}}{k_BT_e(t)}\right)\right)^{-1},\ E_{f(j)}=E_{fd(j)}\left(1-\frac{\pi^2}{12}\left(\frac{k_BT_e(t)}{E_{fd(j)}}\right)^2\right),$$

and $\gamma_{ee(j)}[T_e(t)]=\hbar(\gamma_{a(j)}T_e^2(t)+\gamma_{b(j)}\omega^2)$

(5)

where the summation is composed of M interband terms and each contribution term is denoted by the subscript j, x is the electron energy, κ is a constant related to effective electron mass, E_g is the minimum transition energy from a valence band to an ideal parabolic conduction band, γ_{ee} is the inverse scattering time, $F(x,T_e(t))$ is the electron occupation number, E_f is the electron distribution function, E_{fd} is the transition energy from the band to the Fermi level, k_B is the Boltzman constant, $\hbar$ is the plank constant, and γ_a and γ_b are constant coefficients [24].

The value of the constant coefficients used in the Au permittivity model are listed in Tables 1 and 2. These values were obtained by fitting the measured steady-state permittivity at room temperature [25], $T_l(t) = T_e(t) = 300$ K, with Eqs. (3)-(5). Figure 4 shows the comparison between simulated Au permittivity and that obtained by spectroscopic ellipsometry.

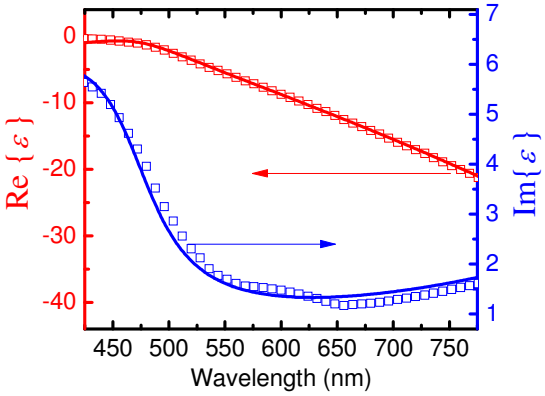

Fig. 4. Comparison of measured (symbols) and simulated (solid lines) complex dielectric permittivity spectra in visible range for fabricated samples **R1.** The dielectric permittivity of Au was modeled as a set of explicit equations (Eqs. (3)-(5)) and compared with measured ellipsometric data.

Table 1. Constant Coefficients of a Au Dielectric Permittivity Model for Intraband Transition Term (Eq. (4))

ε_{intra}	ε_b	$\gamma_0(s^{-1})$	$\gamma_1(s^{-1}k^{-1})$	$\gamma_2(s^{-1}k^{-2})$	$\gamma_3(s^{-3})$	$\omega_p(s^{-1})$
	3.5	1.2×10^{14}	1×10^{10}	2.5×10^{7}	2.1×10^{-18}	1.3×10^{16}

#163236 - $15.00 USD Received 22 Feb 2012; revised 16 Mar 2012; accepted 19 Mar 2012; published 28 Mar 2012

Table 2. Constant Coefficients of a Au Dielectric Permittivity Model of the First and Second Interband Transition Term (Eq. (5)), Respectively

$\varepsilon_{inter(1)}$	$\kappa_{(1)}$	$E_{fd(1)}(eV)$	$E_{f(1)}(eV)$	$\gamma_{a(1)}(s^{-1}k^{-2})$	$\gamma_{b(1)}(s^{-3})$
	100	2.59	1.44	1.2×10^{-4}	1.6×10^{-16}
$\varepsilon_{inter(2)}$	$\kappa_{(2)}$	$E_{fd(2)}(eV)$	$E_{f(2)}(eV)$	$\gamma_{a(2)}(s^{-1}k^{-2})$	$\gamma_{b(2)}(s^{-3})$
	20	3.1	0.5	5.4×10^{-4}	7×10^{-17}

Simulated $\Delta T_{sim}(\lambda, t)$ and $\Delta R_{sim}(\lambda, t)$ are obtained by replacing N_{Au} with $N_{Au}(\lambda, t) = N_{Au} + \Delta N_{sim}(\lambda, t)$ (where $\Delta N_{sim}(\lambda, t) = \Delta n_{sim}(\lambda, t) + i\Delta k_{sim}(\lambda, t)$) in our bilayer linear model 1 (which considers two independent layers). Using this approach and without any further adjustment of the parameters in the model, $\Delta T_{sim}(\lambda, t)$ and $\Delta R_{sim}(\lambda, t)$ closely match with the experimental values. This comparison is shown in Figs. 3(c) and 3(d), where a similar ultrafast temporal evolution is found for all samples. Although better fits could be obtained if small modifications to the value of the electron-phonon coupling rates are introduced to account for its temperature dependence and differences in sample morphology, the model here proposed is sufficient to describe the basic features of the NLO response measured in the bilayers.

In the proposed model, $\Delta N_{sim}(\lambda, t)$ is only ascribed to the Au layer. However, for potential applications in all-optical photonic devices it is useful to derive $\Delta N_{eff} = \Delta n_{eff} + i\Delta k_{eff}$ values which could be ascribed to the entire bilayer. Using a first order approximation, a Taylor expansion of ΔT and ΔR as fuctions of ΔN_{eff} yields the following system of linear equations

$$\begin{aligned}\Delta T &= \frac{\partial T}{\partial n_{eff}}\Delta n_{eff} + \frac{\partial T}{\partial k_{eff}}\Delta k_{eff} \\ \Delta R &= \frac{\partial R}{\partial n_{eff}}\Delta n_{eff} + \frac{\partial R}{\partial k_{eff}}\Delta k_{eff}\end{aligned} \tag{6}$$

In solving this system, ΔN_{eff} is extracted from the experimental data. The partial derivatives, $\partial T/\partial n$, $\partial T/\partial k$, $\partial R/\partial n$ and $\partial R/\partial k$ were approximated by their differentials ($\Delta T/\Delta n_{eff}$, $\Delta T/\Delta k_{eff}$, etc.) by introducing a small perturbation to N_{eff} in the linear model 2.

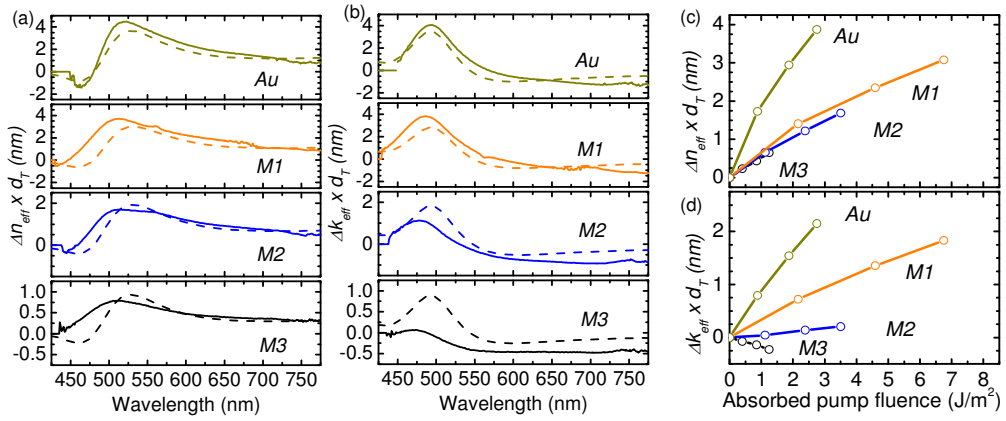

Fig. 5. Spectral dependence of the (a) real and (b) imaginary optical path length change (ΔOPL) pumped at 560 nm with a fluence of 25 J/m^2 for *Au*, *M1*, *M2* and *M3*. Solid line is the extracted $\Delta OPL = \Delta N_{eff} d_T$ and the dashed line is the simulated $\Delta OPL = \Delta N_{sim} d_{Au}$ probed at the peak transmittance delay time; (c) and (d) Absorbed pump fluence dependence of extracted ΔOPL(520 nm) at the peak transmittance change delay time.

#163236 - $15.00 USD Received 22 Feb 2012; revised 16 Mar 2012; accepted 19 Mar 2012; published 28 Mar 2012

Here it is worth pointing out that while it is tempting to establish a direct comparison between ΔN_{eff} and ΔN_{sim}, this is not straight forward for two reasons. First, in our NLO model, ΔN_{sim} is related to the experimental ΔT and ΔR by using linear model 1, while ΔN_{eff} is derived using linear model 2. Second, because in calculating ΔN_{eff} and ΔN_{sim}, the change of refractive index is assumed to occur in layers with different thicknesses, ΔN_{sim} is related only to the thickness of the Au layer (d_{Au}) in the bilayer structure, while ΔN_{eff} is ascribed to the total bilayer thickness (d_T). With these limitations in mind, a comparison can still be made if the change in optical path length ($\Delta OPL = \Delta N_{eff} d_T$ or $\Delta OPL = \Delta N_{sim} d_{Au}$) is used. Figure 5, shows this comparison. In general, good order-of-magnitude estimations of ΔOPL and qualitatively good spectral agreement are obtained using both models. Spectral differences are ascribed to differences in the linear models used. Finally, due to the thermal nature of the NLO response observed in these bilayer films, $\Delta N_{eff}(520\ nm) d_T$ does not follow a linear dependence on the absorbed pump fluence as shown in Fig. 5(c). This trend is consistent with the nonlinear dependence of the electron temperature on the absorbed fluence. Furthermore, even at the same absorbed power, the NLO response of a single *Au* layer is larger than any of the bilayers *M1*, *M2* and *M3.*

3. Conclusion

The optical properties of Ag/Au bilayer metallic thin films with a total thickness of approximately 20 nm and with different Ag/Au mass-thickness ratios were studied. The effective refractive index values were found to be spectrally tunable by controlling the mass-thickness ratio between Au and Ag. Hence, the optical loss introduced by interband transitions in Au layers can be reduced. As a consequence, improvement of the quality factors (Q_{LSP} and Q_{SPP}) derived for plasmonic applications and the potential transmittance (Ψ) for optical filter applications are calculated within the visible range. These spectral shifts also lead to similar spectral shifts on the NLO response of the bilayers. The NLO response is shown to be ultrafast and comparable in origin and magnitude to that observed in single Au films. The NLO response in the bilayer films is dominated by the ultrafast dynamics of the thermal exchange between the absorbed optical field and the electron cloud and the lattice in the Au layer. The combined properties of these bilayers could therefore be attractive for a variety of linear and nonlinear photonic applications.

Acknowledgments

This work was partially funded by NSF through STC-DMR-0120967, by ARO through contract/ grant 50372-CH-MUR, by AFOSR (BIONIC Center grant No. FA9550-09-1-0162), and AFOSR (grant No. FA9550-09-1-0418).

#163236 - $15.00 USD Received 22 Feb 2012; revised 16 Mar 2012; accepted 19 Mar 2012; published 28 Mar 2012